High-Accuracy Real-Time Attitude Determination and Imagery Positioning System for Satellite-Based Remote Sensing

Xuedi Chen, *Graduate Student Member, IEEE*, Haiyang Zhan, Shaoyan Fan, Qilong Rao, Zhenqiang Hong, Zheng You, Fei Xing, and Chunyu Liu

***Abstract*— The precise attitude determination and imagery positioning is crucial for remote sensing satellites to accomplish diverse observation missions. However, the complex fluctuations of environmental conditions result in severe and time-variant camera misalignment, which degrades the inertial attitude determination precision of optical payloads greatly and further hinders the improvement of positioning accuracy. Here, we develop a high-accuracy real-time attitude determination and imagery positioning system. With multiple laser sources integrated on the camera focal plane and a retroreflector reflecting the laser into a star tracker, the active optical monitoring path between the camera and the star tracker is constructed and provides the ability to monitor the camera misalignment. Using a dichroic mirror, the star tracker can detect the stars and the laser simultaneously. Then, the camera attitude determination and imagery positioning model based on the "star–laser" joint detection is established, which can precisely monitor the camera misalignment by the laser imaging and determine the inertial camera attitude combined with the star imaging. The ground simulation experiment is conducted and the results demonstrate the accuracy and effectiveness of the proposed method in monitoring the camera misalignment. Therefore, the proposed method provides an innovative idea for high-accuracy positioning.**

***Index Terms*— Camera attitude determination, camera misalignment monitoring, geometric positioning, SVGF-1 satellite.**

Manuscript received 26 June 2023; revised 1 September 2023; accepted 13 September 2023. Date of publication 18 September 2023; date of current version 3 October 2023. This work was supported in part by the National Natural Science Foundation of China under Grant 51827806 and Grant U21A6003, in part by the Tencent Foundation under the Xplorer Prize, and in part by the Shanghai Academy of Spaceflight Technology under Grant SAST2022-038. *(Corresponding authors: Fei Xing; Chunyu Liu.)*

Xuedi Chen, Haiyang Zhan, Shaoyan Fan, and Fei Xing are with the Beijing Advanced Innovation Center for Integrated Circuits, Tsinghua Univeristy, Beijing 100084, China, also with the State Key Laboratory of Precision Measurement Technology and Instruments, Tsinghua University, Beijing 100084, China, and also with the Department of Precision Instrument, Tsinghua University, Beijing 100084, China (e-mail: cxd18@mails.tsinghua.edu.cn; hbyszhy@163.com; fsy18@mails.tsinghua.edu.cn; xingfei@mail.tsinghua.edu.cn).

Qilong Rao and Zhenqiang Hong are with the Shanghai Academy of Spaceflight Technology, Shanghai 201109, China (e-mail: mrrao2561@126.com; hongzhenqiang2023@163.com).

Zheng You was with the Beijing Advanced Innovation Center for Integrated Circuits, Department of Presicion Instrument, State Key Laboratory of Precision Measurement Technology and Instruments, Tsinghua University, Beijing 100084, China. He is now with School of Mechanical Science and Engineering, Huazhong University of Science and Technology, Wuhan 430074, China (e-mail: yz-dpi@mail.tsinghua.edu.cn).

Chunyu Liu is with the Changchun Institute of Optics, Fine Mechanics and Physics, Chinese Academy of Sciences, Changchun 130033, China (e-mail: mmliucy@163.com).

Digital Object Identifier 10.1109/TGRS.2023.3316151

I. Introduction

REMOTE sensing technology has been widely used in multiple fields, such as Earth observation, space surveillance, and scientific exploration [1], [2]. High-accuracy imagery positioning is the core goal of remote sensing and largely depends on the correctness of internal parameters of camera and the measurement precision of inertial camera attitude. The inertial camera attitude is calculated by combining the attitude data from a star tracker and the alignment matrix between camera and star tracker [3], [4], [5]. The alignment matrix is the external parameter of the camera and is calibrated strictly on the ground. However, the vibration during the satellite launching and the thermal fluctuation during the on-orbit operation, especially the latter, will cause noticeable and variable deviation in the alignment matrix, which may reach dozens of arc seconds [6], [7]. Currently, the attitude measurement accuracy of star trackers can achieve about $1''$ (1σ) easily [8]. Therefore, camera misalignment is a main factor to limit the accuracy of imagery positioning, and it is necessary to monitor the camera alignment on orbit for high-accuracy imagery positioning.

Most of the traditional methods to determine the camera alignment are based on the on-orbit geometric calibration with control points (CPs), such as ground control points (GCPs) and stars [9], [10], [11]. The calibrated value of the external installation matrix is used for the image positioning before the next calibration. The IKONOS satellite was the first commercial remote sensing satellite with 1m resolution. It used a set of independent images of the knife-edge targets for the external calibration, and the stereo positioning accuracy without GCPs was 7.9m (CE90) in horizontal and 7.6m (LE90) in elevation [12], [13]. For the ZiYuan-3 satellite, the abundant GCPs were calibrated by matching the images with the reference data from digital orthophoto map (DOM). Combining with the attitude data of the satellite, the camera alignment was calibrated. Then, the uncontrolled positioning accuracy was about 10m (RMSE) [4], [14]. Xing et al. [15] used the stars as the CPs for conducting the external calibration with the Jilin-1 SP07. The error of the external parameters was within $\pm 1.4''$. These calibration-based methods can provide reliable and accurate external installation. However, the calibrated external parameters can only demonstrate the status of the remote sensing camera at the calibration time rather than during the observation process.

Hence, the fit-based methods for analyzing the camera misalignment trends were studied by some scholars. By gathering

the statistics of the external parameters, the fitting model of the external parameters changing trend is established for extrapolation. Takaku and Tadono [16] developed an alignment changing trend model for predicting the camera misalignment of ALOS satellites. Linear models were applied for the long-term change, and second-degree Fourier series were applied for the short-term change [16]. Li et al. [17] proposed to use the third-order Fourier series to fit the change of positioning error in each cycle of the orbit. Through the linear combination of the Fourier series fitting models of three consecutive orbits, the error of next orbital period was extrapolated. These methods can effectively correct the error of the external installation matrix throughout the entire process of satellite operation, but they can hardly realize the high-accuracy determination of the camera alignment due to the complexity of the actual situation.

Furthermore, the bundle block adjustment was used to estimate the external parameters and to actualize the photogrammetry without GCPs. Wang and Wang [19] developed the equivalent frame photo (EFP) multifunctional bundle adjustment technique for the three-line CCD cameras in Tianhui-1 satellite. The technique added the compensation term of the error of external parameters in the bundle adjustment for estimating and correcting the external parameters. The method can realize the high-accuracy determination of the external installation matrix between camera and star trackers [18], [19], [20]. However, the method is based on the intersection of three-line CCD cameras. The algorithm is very complex and the computational cost is high.

The above methods have their own shortcomings and are hard to actualize the high-accuracy real-time determination of attitude and position. The main obstacle is that it is hard to monitor the camera alignment matrix precisely because the only way for coupling with camera and star tracker is the mechanical fixation. Recently, the methods to directly monitor the inertial attitude of the payloads were developed. The Ice, Cloud and land Elevation Satellite-2 (ICESat-2) equipped with a laser payload and used a laser reference system (LRS) for realizing the joint imaging of the laser and the stars on a back-to-back detector [21], [22]. Hence, the outgoing laser pointing vector in inertial space was determined accurately. Actually, compared with the laser payload, the remote sensing camera can only passively receive rather than actively transmit optical signals, which limits the application of method in remote sensing satellites. However, the real-time monitoring of camera misalignment and high-accuracy determination of attitude and position are desired by some satellite users, such as Shanghai Academy of Spaceflight Technology (SAST).

The SVGF-1 satellite is a commercial remote sensing satellite developed by SAST and is scheduled to be launched in 2024. The satellite is equipped with a high-resolution camera and high-accuracy star trackers. The main characteristics of the camera and star trackers are shown in Table I. The camera on board consists of a panchromatic sensor with a spatial resolution of 0.25m and a multispectral sensor with 1m resolution. The high-accuracy star trackers on board are characterized by excellent dynamic performance, high update rate, and high precision. These devices will devote effort to realize the high-accuracy determination of accuracy and position. However, as mentioned above, the misalignment between camera and star trackers mainly leads to positioning errors and we can only make very limited efforts to monitor the misalignment.

TABLE I
MAIN CHARACTERISTICS OF CAMERA AND STAR TRACKERS IN SVGF-1

Items			Value
Camera	Panchromatic sensor	Focal length	14m
		Pixel size	7μm
		Spectral range	450~800nm
		Ground resolution	0.25m
	Multispectral sensor	Focal length	14m
		Pixel size	28μm
		Spectral range	B1:450~520nm B2:520~590nm B3:630~690nm B4:770~890nm
		Ground resolution	1m
Star tracker		Pointing accuracy	$< 1''(3\sigma)$
		Update rate	10Hz
		FOV	15°×15°

Inspired by the method used in ICESat-2, we develop a high-accuracy real-time determination system of attitude and position (DSAP) for SVGF-1 in this article. The concept of the system is to add an active fiducial optical path to couple the camera and the star tracker for realizing the monitoring of the camera misalignment. First, the theory and design of the high-accuracy real-time determination system of attitude and position are introduced in Section II, and then, the camera attitude determination and imagery positioning model based on the "star–laser" joint detection is established in Section III. Finally, a ground verification experiment platform is elaborated and the experimental results demonstrate the accuracy and effectiveness of the proposed method in Sections IV and V, respectively.

II. HIGH-ACCURACY REAL-TIME DETERMINATION SYSTEM OF ATTITUDE AND POSITION

A. Imagery Positioning Geometric Model

The core goal of satellite-based remote sensing is to realize the high-accuracy imagery positioning. The strict imaging geometric model is the basis for imagery positioning, as shown in Fig. 1(a). The imagery positioning geometric model of SVGF-1 is established as follows:

$$\begin{bmatrix} X \\ Y \\ Z \end{bmatrix}_{\mathrm{WGS84}} = \begin{bmatrix} X_S \\ Y_S \\ Z_S \end{bmatrix}_{\mathrm{WGS84}} + m R_{J2000}^{\mathrm{WGS84}} R_{\mathrm{star}}^{J2000} R_U R_{\mathrm{cam}}^{\mathrm{star}} \begin{bmatrix} X - X_0 - \Delta X \\ Y - Y_0 - \Delta Y \\ -f_{\mathrm{cam}} \end{bmatrix} \tag{1}$$

where $[\,X\ Y\ Z\,]'_{\mathrm{WGS84}}$ denotes the position vector of an observed target in the WGS84 geocentric coordinate system. The goal of remote sensing is to determine $[\,X\ Y\ Z\,]'_{\mathrm{WGS84}}$ accurately. $[\,X_S\ Y_S\ Z_S\,]'_{\mathrm{WGS84}}$ is the position vector of the remote sensing satellite in the WGS84 system, which can be

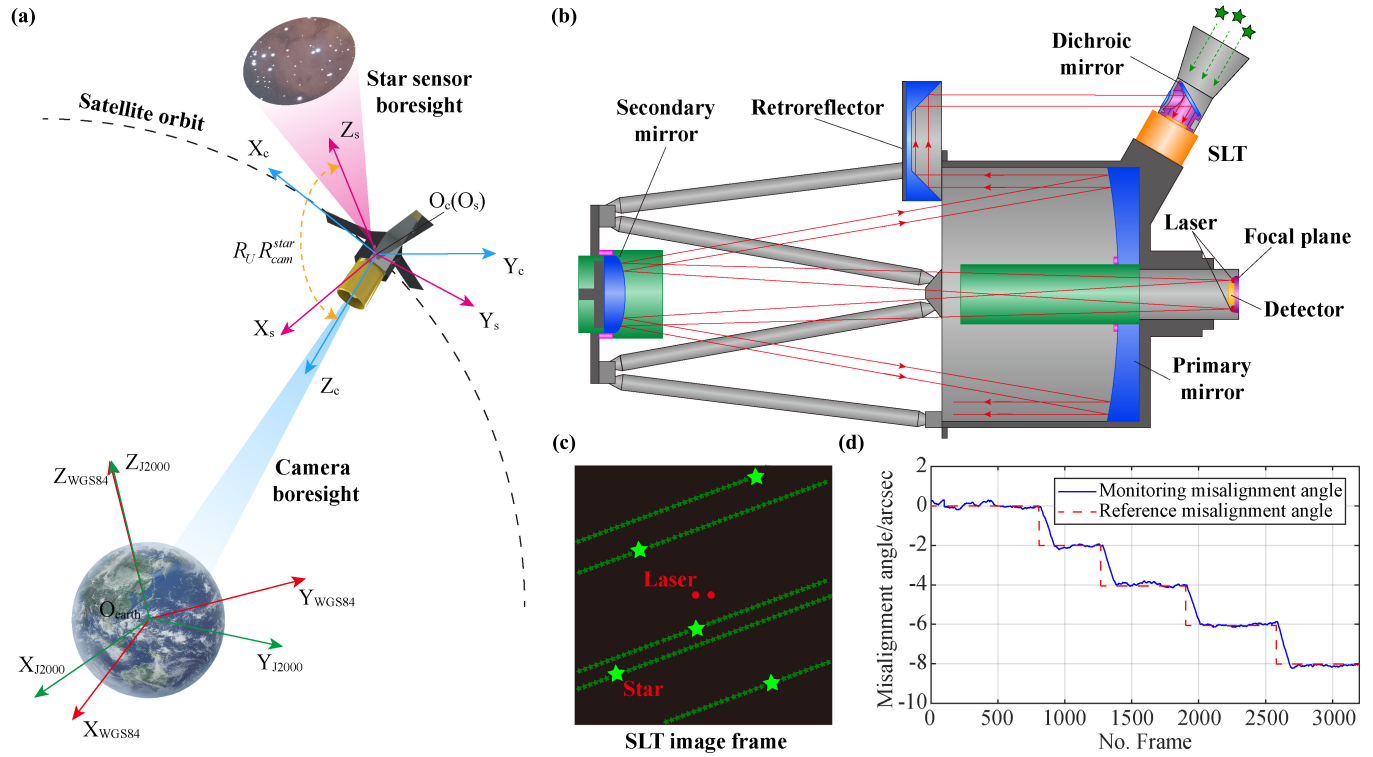

Fig. 1. (a) Diagram of the imagery positioning geometric model. O_{Earth}-$X_{\text{WGS84}}Y_{\text{WGS84}}Z_{\text{WGS84}}$ is the WGS84 geocentric coordinate system. O_{Earth}-$X_{J2000}Y_{J2000}Z_{J2000}$ is the J2000 coordinate system. O_s-$_sY_sZ_s$ is the coordinate system of star tracker. O_c-$X_cY_cZ_c$ is the coordinate system of camera. (b) The illustration of the DSAP. (c) Diagram and image frame of the SLT. The red spots denote the laser imagery, and the green markers indicate the star imagery. (d) Experimental result of monitoring misalignment angle through the proposed system and method. The blue line indicates the monitoring misalignment angle, and the red dashed line denotes the reference misalignment angle.

obtained by the global positioning system (GPS). Generally, the accuracy of the satellite position is very high and can reach the centimeter level. m is the scaling factor. R_{J2000}^{WGS84} indicates the transformation matrix from the J2000 coordinate system to the WGS84 system. R_{star}^{J2000} represents the transformation matrix from the star tracker to the J2000 system, which can be measured by the star tracker. Currently, even commercial star trackers can achieve an accuracy of $1''$. $R_{\text{cam}}^{\text{star}}$ is the alignment matrix between the remote sensing camera and the star tracker, which is calibrated strictly before the launching of satellite. (X, Y) denotes the image coordinates of the observed target in the camera imaging coordinate system. (X_0, Y_0) is the coordinate of the principal point, and f_{cam} is the focal length of the camera. $(\Delta X, \Delta Y)$ indicates the deviation of target coordinates caused by the internal distortion, which will be calibrated strictly based on the geometric positioning field.

R_U is the misalignment matrix between the camera and the star tracker. The changing trend of R_U is time-variant and complex due to the fluctuations of environmental conditions, especially the thermal environment. It is hard for satellites to monitor the change of R_U, and the errors of R_U mainly lead to severe positioning errors for the SVGF-1. Therefore, the DSAP is established and an additional measurement optical path is added between the camera and the star tracker to address this key problem.

B. DSAP

The concept of the system is to add an active fiducial optical path to couple camera and star tracker for realizing the monitoring of camera misalignment. The conceptual diagram of the DSAP is shown in Fig. 1(b). The DSAP in the SVGF-1 satellite consists of a laser and detector integrated (LDI) focal plane, a star and laser tracker (SLT), and a retroreflector, as shown in Fig. 2(a). The LDI focal plane with the remote sensing camera can not only detect the Earth light for the observation missions but also simultaneously emit laser light. The retroreflector is necessary to reflect the collimated laser light from the camera into the optical system of SLT. The SLT is used to detect the imagery of the lasers and stars at the same time, as shown in Fig. 1(c). The imagery of the laser contains the information of the camera misalignment. When the camera and the SLT are misaligned, the position of the laser points will change in response. The SLT can measure the coordinate changes of the laser points for calculating the camera misalignment accurately, as shown in Fig. 1(d). Then, the SLT can also conduct the star image processing for obtaining the attitude information such as a traditional star tracker. Combining with the two terms, the camera attitude in inertial space can be determined accurately. Finally, the fiducial monitoring optical path between the camera and the star tracker is constructed. The three main parts of DSAP will be described next in detail.

1) LDI Focal Plane: The structure of the LDI focal plane in the SVGF-1 satellite is shown in Fig. 2(b). The focal plane is composed of the combination of 14 detectors. The focal plane is designed as an L-shape and the detectors are distributed on two vertical planes. The reflectors are used for the combination of detectors. In the LDI focal plane, multiple laser sources are

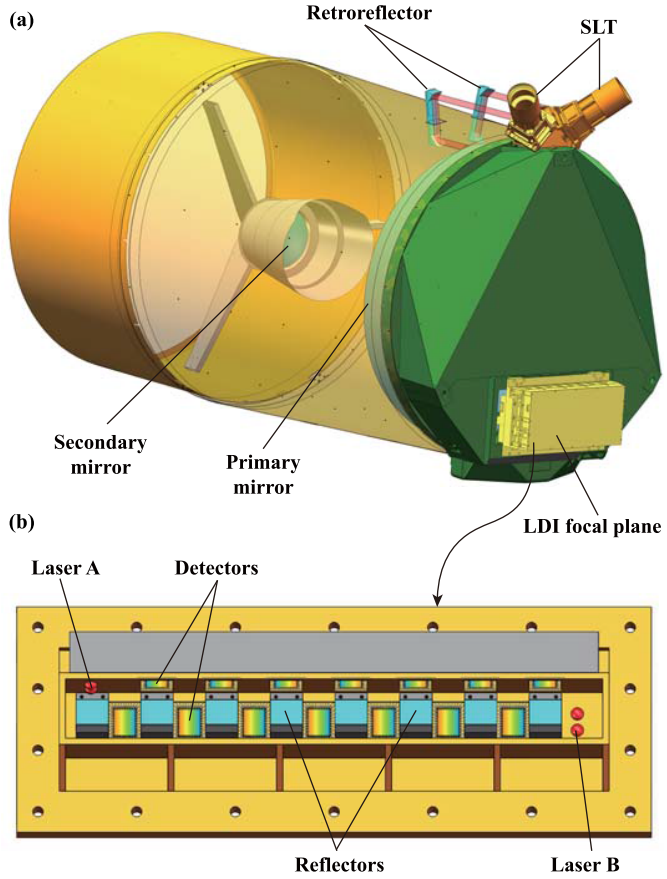

Fig. 2. (a) Structural diagram of the DSAP in SVGF-1 satellite. (b) Structural diagram of the LDI focal plane. The colored squares indicate the detectors, and the blue cubes denote the reflectors.

also mounted on the focal plane, which means that the laser light will be collimated into parallel light by the camera's optical system. Thus, the LDI focal plane provides the camera with the capability to actively emit the laser light carrying the information of camera misalignment.

It is worth noting that the laser light cannot affect the normal imaging of the camera, especially when the lasers are mounted at the focal plane of camera. Therefore, the divergence angle of the lasers is controlled strictly and matches the aperture angle of the camera. It makes sure that the laser light does not illuminate the internal structure of camera and results in the reflected stray light. Moreover, it is inevitable that the laser luminescence will generate heat and cause the thermal-induced displacement of laser sources. Fortunately, the focal length of the camera is 280 times that of the SLT in our work, which means that the displacement of laser on the SLT detector will be reduced by 280 times. Meanwhile, the support of the laser is made of a material with low linear expansion coefficient and the thermal control system strictly controls the temperature fluctuation of the focal plane. Thus, it is reasonable to ignore the influence of the thermal-induced displacement of laser sources.

As shown in Fig. 2(b), the multiple laser sources should not be in close proximity to each other. In the DSAP, the laser will be detected by the SLT. Generally, the focal length of the camera is much longer than that of the SLT, which means that the close installation of laser sources will cause the laser spots in the SLT frame to be too near to distinguish each other.

2) Retroreflector: Generally, the remote sensing camera and star trackers are mounted in opposite directions, with the camera pointing to the nadir and the star trackers pointing to the zenith. The retroreflector can reflect the light back 180° toward the incident direction, which is the best candidate to reflect the laser into the SLT. Furthermore, regardless of the three-dimensional (3-D) rotation of the retroreflector, the direction of emergent light does not change. It demonstrates that the misalignment of retroreflector is not coupled with the camera misalignment and guarantees the benchmark of the measurement optical path. In SVGF-1, the retroreflector is set to the right angle conical mirror.

3) SLT: The SLT is developed by our team and TY-Space Technology (Beijing) Ltd. The structural diagram of the SLT in SVGF-1 is shown in Fig. 3(a), and the SLT consists of baffle, optical reflective structure, and the processor shell. The narrow bandpass filter (NBPF), the dichroic mirror (DM), and the invar support compose the optical reflective structure, which is the core part of SLT for realizing the simultaneous detection of the stars and the laser, as shown in Fig. 3(b). The concept relies on the selective transmission and reflection characteristics of DMs for light with different wavelengths. Generally, the spectrum of star light detected by star trackers is the visible spectrum. Thus, the wavelength of the laser should be separated from the visible spectrum and is set to 850nm. The transmission and reflection properties of the DM should be designed carefully, as shown in Fig. 3(c). The transmission band is from 400 to 800nm and the reflection band is from 840 to 1050nm. The visible star light will pass through the DM and the 850nm laser will be reflected. Both two lights are detected at the same time for monitoring the camera misalignment and determining the attitude of the SLT. Furthermore, to ensure the normal star imaging of SLT and the monitoring accuracy of the camera misalignment, lots of efforts have been made to resist the disturbance from the stray light and the thermal deformation.

For the SLT, the stray light mainly stems from the Sun, the Earth, and the remote sensing camera. The function of the baffle is similar to that of the traditional star tracker and is to suppress stray light from the Sun and the Earth. However, the optical reflective structure occupies the space of the aperture in the traditional baffle, which is shown in Fig. 3(b). Thus, the aperture of the baffle should be designed carefully to provide installation space for the optical reflective structure and to maintain the original stray light resistance ability. The stray light from the remote sensing camera is the landscape light reflected by the primary mirror and the retroreflector into the SLT. The NBPF is used to reduce the influence of the stray light. The NBPF is installed in the baffle support and is designed to only transmit the 850nm light and to reject all other wavelengths of the light, as shown in Fig. 3(c). Therefore, the 850nm laser will pass through the NBPF and the most of stray light from the remote sensing camera will be rejected.

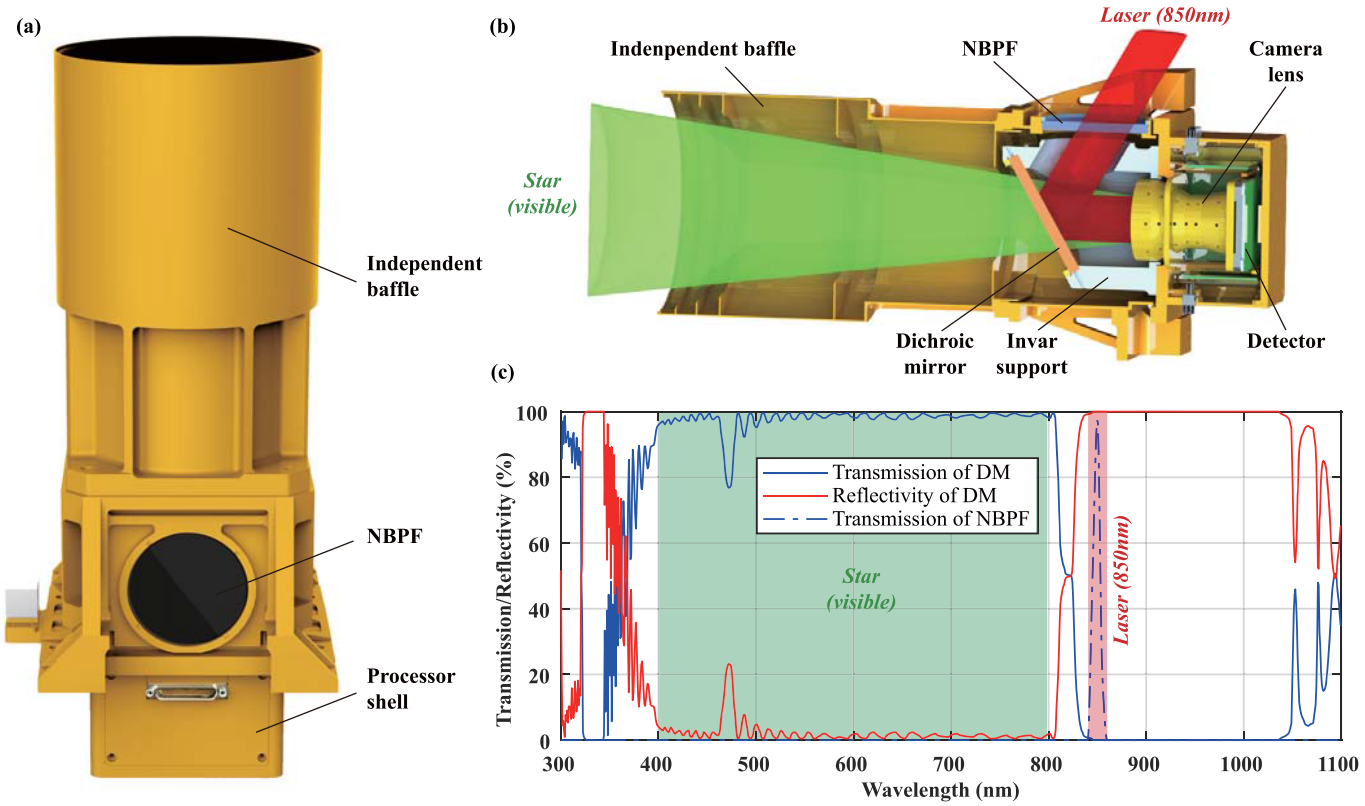

Fig. 3. (a) Structural diagram of the SLT. (b) Optical paths of the visible star and 850nm laser into the SLT. The star light is described by the green part and the laser light is described by the red part. (c) Transmission and reflectivity of the DM and the NBPF. The green area represents the visible spectral range of the star and the red area represents the 850nm spectral range of the laser.

The DM is the reflector for the laser and the core part of the active optical fiducial system. The monitoring accuracy is extremely sensitive to the misalignment of the DM. Therefore, the satellite thermal control system should ensure that the temperature of the SLT is stable. Furthermore, the support of the DM is made of invar, of which the linear expansion coefficient is very small and is about 1×10^{-6}/°C. An independent baffle is designed and utilized in the SLT to ensure thermal stability. Traditionally, the baffle and the lens are mounted on the same structural plate of the star tracker, which means that the thermal deformation of the baffle will affect the optical system. In the SLT, the baffle is installed in the satellite platform and is independent of other parts of the SLT. The influence of the thermal deformation of the baffle is isolated from the optical system. The independent baffle also reduces the design difficulty of the thermal control system.

By the DSAP, the remote sensing camera has the potential to monitor the camera misalignment for high-accuracy attitude determination and imagery positioning.

III. Attitude and Position Determination Model Based on "Star–Laser" Joint Detection

Based on the DSAP in SVGF-1, the SLT can detect the star and the laser at the same time. The laser imagery includes the information of the camera misalignment and the star imagery can provide the attitude data. Here, the camera attitude determination and imagery positioning model based on the "star–laser" joint detection is proposed.

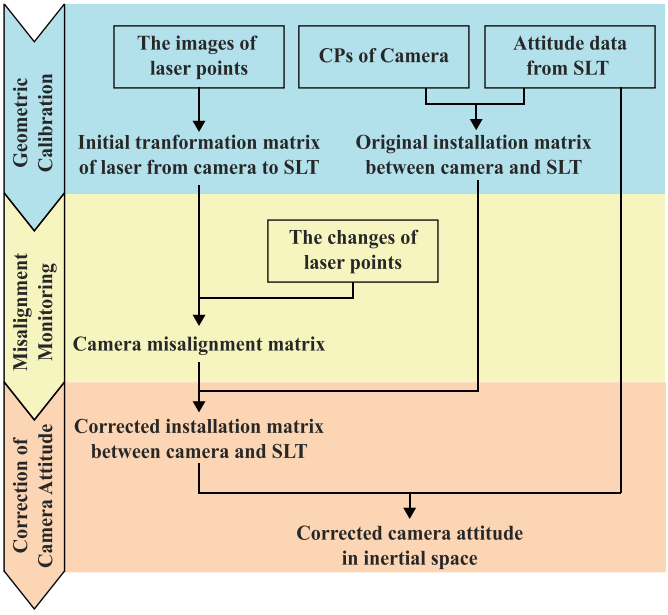

Fig. 4. Technical route of the misalignment monitoring and correction method based on "star–laser" joint detection.

The technical route of the method is shown in Fig. 4 and consists of three main steps: the geometric calibration, the misalignment monitoring, and the correction of camera attitude

1) *Geometric Calibration:* The traditional geometric calibration is conducted. By combining the CPs of camera

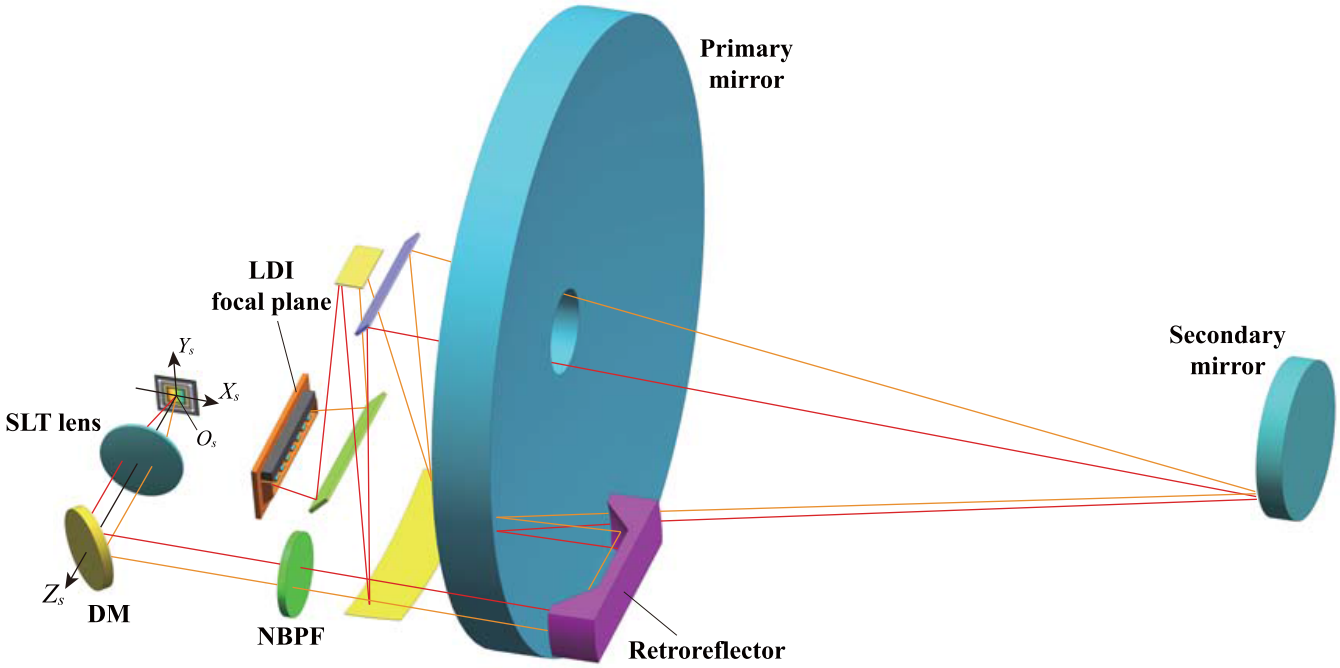

Fig. 5. Transformation relationship of laser from camera to SLT.

and the attitude data from SLT, the original installation matrix between camera and SLT is calibrated. Meanwhile, the position of laser in the SLT image frame is extracted, based on which the transformation matrix of laser from camera to SLT can be obtained with the reference position of laser in the camera focal plane.

2) *Misalignment Monitoring:* In this step, the position changes of laser points in SLT image frames are detected continuously. By combining the transformation matrix of laser from camera to SLT, the camera misalignment matrix can be updated constantly in real time.
3) *Correction of Camera Attitude:* With the camera misalignment matrix, the original installation matrix can be corrected. Coupled to the attitude data from SLT, the camera pointing in inertial space can be acquired.

Next, the attitude and position determination model based on "star–laser" joint detection will be described in detail.

A. Laser Transformation Model From Camera to SLT

The optical path of laser is used to couple the camera and SLT to provide the possibility of misalignment monitoring. Thus, the laser transformation model from camera to SLT is the foundation of the method, of which the diagram is shown in Fig. 5.

As shown in Fig. 5, we define the camera coordinate system with O_c-$X_cY_cZ_c$. The origin O_c is the intersection of the camera optical axis and the focal plane. $\boldsymbol{v}_{i,\mathrm{cam}}$ is the emitted vector of laser source i in the camera coordinate system and is represented as

$$\boldsymbol{v}_{i,\mathrm{cam}} = \frac{1}{\sqrt{(X_i - X_0)^2 + (Y_i - Y_0)^2 + f_{\mathrm{cam}}^2}} \begin{bmatrix} -(X_i - X_0) \\ -(Y_i - Y_0) \\ f_{\mathrm{cam}} \end{bmatrix} \tag{2}$$

where (X_i, Y_i) denotes the coordinates of laser source i in the camera focal plane. The position of the laser sources in camera focal plane can be obtained by the design value. f_{cam} is the focal length of the camera.

The emitted vectors of laser sources are reflected by the retroreflector into the SLT. Then, the lasers are reflected by the DM of the SLT into the imaging system. We define the SLT coordinate system with O_s-$X_sY_sZ_s$. f_s is the focal length of the SLT and the origin O_s denotes the intersection of the SLT optical axis and the SLT focal plane. $\boldsymbol{w}_i^k$ is the received vector of laser source i in the SLT coordinate system at the kth frame and is represented as

$$\boldsymbol{w}_i^k = \frac{1}{\sqrt{\left(x_i^k - x_0\right)^2 + \left(y_i^k - y_0\right)^2 + f_s^2}} \begin{bmatrix} -\left(x_i^k - x_0\right) \\ -\left(y_i^k - y_0\right) \\ f_s \end{bmatrix} \tag{3}$$

where (x_i^k, y_i^k) denotes the imaging coordinates of laser source i at the kth SLT image frame, which can be extracted by the centroiding algorithm, and (x_0, y_0) is the coordinates of the principal point of the SLT.

Therefore, the transformation relationship of $\boldsymbol{v}_{i,\mathrm{cam}}$ and $\boldsymbol{w}_i^k$ can be derived in theory as follows:

$$\boldsymbol{v}_{i,\mathrm{cam}} = \left(\boldsymbol{T}_{\mathrm{cam}}^{\mathrm{st}}\right)' \boldsymbol{w}_i^k \tag{4}$$

and the laser transformation matrix $\boldsymbol{T}_{\mathrm{cam}}^{\mathrm{st}}$ can be calculated according to the least-square theory as follows:

$$\min_{\boldsymbol{T}_{\mathrm{cam}}^{\mathrm{st}}} \sum_{k=1}^{M} \sum_{i=1}^{N} \left\| \boldsymbol{v}_{i,\mathrm{cam}} - \left(\boldsymbol{T}_{\mathrm{cam}}^{\mathrm{st}}\right)' \boldsymbol{w}_i^k \right\|^2 \tag{5}$$

where N is the number of laser sources and M is the number of the image frame. In this application, M is set to 100 for suppressing the influence of random error. The algorithm to

calculate (5) is the quaternion estimator (QUEST), which is very mature and can be implemented in real time [23], [24].

To suppress the influence of the random error in the laser extraction, the laser images from multiple consecutive frames are used for calculating (5). Generally, the frame rate of the SLT is 10Hz, which means that the capture time of 100 images is about 10s. Actually, the external installation matrix between camera and SLT changes slowly. The multiple-frame smooth filtering is reasonable and effective.

B. Misalignment Monitoring Model

Camera misalignment monitoring is the measurement of the relative changes in the installation matrix between camera and SLT. Thus, the zero point of the monitoring is the first thing we should do.

In the geometric calibration phase, the original installation matrix between camera and SLT $\boldsymbol{R}_{\text{st}}^{\text{cam},0}$ can be calibrated by the CPs based on the geometric calibration method. Meanwhile, the imaging coordinates of laser source i at the kth SLT image frame are detected and are represented as $(x_{i,0}^k, y_{i,0}^k)$. Hence, the received vector of laser source i in the SLT coordinate system during the geometric calibration $\boldsymbol{w}_{i,0}^k$ can be obtained by (3). The original laser transformation matrix $\boldsymbol{T}_{\text{cam},0}^{\text{st}}$ can be calculated by substituting $\boldsymbol{w}_{i,0}^k$ into (5).

During the misalignment monitoring phase, the camera misalignment causes the change of the imaging coordinates of laser sources in SLT. The imaging coordinates of laser source i in SLT at arbitrary time t can be obtained by the centroiding method and are represented as $(x_{i,t}^k, y_{i,t}^k)$. According to (3), the received vector of laser source i in the SLT coordinate system at arbitrary time t $\boldsymbol{w}_{i,t}^k$ is calculated.

It is worth noting that the emitted vectors of laser sources in the camera coordinate system are constant regardless of the camera misalignment. According to (4), the transformation relationship of the $\boldsymbol{v}_{i,\text{cam}}$ and the received vector of laser source i in the SLT coordinate system at time t $\boldsymbol{w}_{i,t}^k$ can be derived by the laser transformation matrix from camera to SLT at time t $\boldsymbol{T}_{\text{cam},t}^{\text{st}}$. $\boldsymbol{T}_{\text{cam},t}^{\text{st}}$ can be calculated by (5).

The misalignment causes the change of the laser transformation matrix. Therefore, the camera misalignment matrix $\boldsymbol{R}_{\text{cam},0}^{\text{cam},t}$ can be formulated as follows:

$$\boldsymbol{T}_{\text{cam},t}^{\text{st}} = \boldsymbol{T}_{\text{cam},0}^{\text{st}} \left(\boldsymbol{R}_{\text{cam},0}^{\text{cam},t}\right)'. \tag{6}$$

Thus, (5) can be expanded as follows for calculating the camera misalignment matrix $\boldsymbol{R}_{\text{cam},0}^{\text{cam},t}$:

$$\min_{\boldsymbol{R}_{\text{cam},0}^{\text{cam},t}} \sum_{k=1}^{M} \sum_{i=1}^{N} \left\| \boldsymbol{v}_{i,\text{cam}} - \boldsymbol{R}_{\text{cam},0}^{\text{cam},t} \left(\boldsymbol{T}_{\text{cam},0}^{\text{st}}\right)' \boldsymbol{w}_{i,t}^k \right\|^2. \tag{7}$$

C. Correction Model of Camera Attitude

The core goal of the proposed method is to determine the inertial attitude of camera. The coordinate change of laser imagery provides the information of the misalignment. Then, the misalignment should be corrected.

The original installation matrix between camera and SLT $\boldsymbol{R}_{\text{cam},0}^{\text{st}}$ is calibrated in the phase of geometric calibration, and the camera misalignment matrix at arbitrary time t is calculated in the phase of misalignment monitoring. Thus, the corrected installation matrix between camera and SLT $\boldsymbol{R}_{\text{st}}^{\text{cam},t}$ can be formulated as follows:

$$\boldsymbol{R}_{\text{st}}^{\text{cam},t} = \boldsymbol{R}_{\text{cam},0}^{\text{cam},t} \boldsymbol{R}_{\text{st}}^{\text{cam},0}. \tag{8}$$

The SLT can detect the laser and the stars at the same time, which means that the SLT can calculate the attitude matrix at time t $\boldsymbol{R}_{\text{inertial}}^{\text{st},t}$. Combining $\boldsymbol{R}_{\text{inertial}}^{\text{st},t}$ with the corrected installation matrix at time t, the corrected pointing of the camera boresight in inertial space can be represented as follows:

$$\boldsymbol{R}_{\text{inertial}}^{\text{cam},t} = \boldsymbol{R}_{\text{st}}^{\text{cam},t} \boldsymbol{R}_{\text{inertial}}^{\text{st},t}. \tag{9}$$

Finally, the corrected inertial attitude of the camera $\boldsymbol{R}_{\text{inertial}}^{\text{cam},t}$ is obtained and can be used for high-accuracy positioning.

IV. Experiment

The proposed method has been applied to the SVGF-1, and the on-orbit verification experiment will be conducted after launch. Before the launch, our proposed method, as an innovation technology, must be validated for its accuracy and effectiveness. Therefore, we build the ground DSAP verification platform and conduct the accuracy and effectiveness validation experiment.

A. Ground DSAP Verification Platform

Fig. 6 shows the ground DSAP verification platform. Four 850nm laser sources are mounted on a piezoelectric micro-motion table as shown in Fig. 6(a), of which the diagonal installation distance is 22mm. The laser plane is set on the focal plane of a telescope. According to that, the emitted vectors of laser sources in camera coordinates are determined. The piezoelectric micro-motion table can drive the laser plane to move along both X- and Y-directions at the micrometer level. Actually, the camera misalignment angle (MA) is equivalent to the motion of the focal plane, and the relationship of them can be formulated as follows:

$$\theta_{X/Y} = -\tan\left(L_{Y/X}\right) \cdot f_{\text{cam}} \tag{10}$$

where $\theta_{X/Y}$ denotes the camera MA along the direction of the X- or Y-axis and $L_{Y/X}$ is the translation value of the focal plane along the Y- or X-axis.

The telescope is used to imitate the optical system of remote sensing camera and to collimate the light from laser sources to parallel light. In order to facilitate the construction of the ground system, the telescope is a truss-type Ritchey–Chretien telescope. A reflector is utilized to reflect the collimated laser light into the SLT. Due to the high difficulty in manufacturing the right angle conical mirror, the reflector in the ground DSAP platform is the reflective structure composed of two mirrors installed at the right angle. We believe that there is no thermal deformation in the reflector during a short time and the reflector will not bring influence on the misalignment monitoring.

The SLT is developed from the NST-10 DS star tracker manufactured by TY-Space Technology (Beijing) Ltd. The installation of SLT is consistent with that in SVGF-1. The included

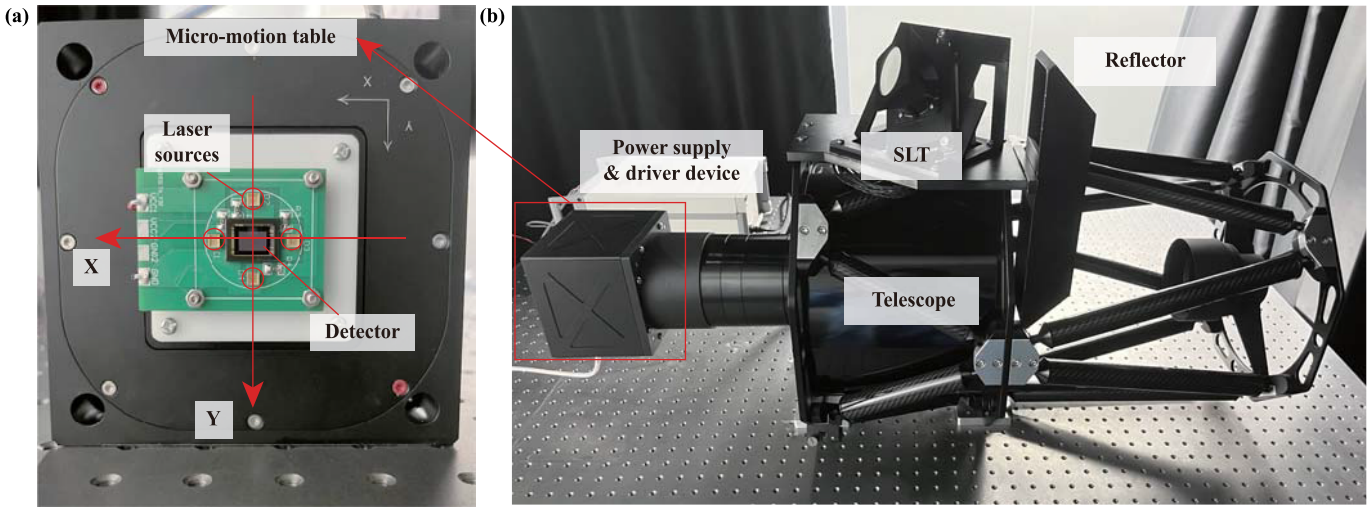

Fig. 6. (a) Diagram and installation configuration of the micro-motion table and the 850nm laser sources. The red circles indicate the laser sources. The X- and Y-axes denote the motion directions of the micro-motion table and the axes of camera coordinate system. (b) Diagram of ground DSAP verification platform. The red rectangular box indicates the camera focal plane, which contains the micro-motion table and the 850nm laser sources.

TABLE II
PARAMETERS OF THE GROUND DSAP PLATFORM

Item		Value
Piezoelectric micro-motion table	Maximum travel	100μm
	Resolution	3.5nm
Laser source	Number	4
	Wavelength	850nm
Telescope	Focal length	2000mm(nominal)
SLT	The transmission range of DM	400-775nm (Tavg>90%)
	The reflectivity range of DM	840-1050nm (Ravg>98%)
	Focal length	60mm
	Resolution	1024 ×1024
	Pixel size	13μm
	Angular resolution	44.6″
	Imaging spectrum range	500-1000nm

angle between the camera boresight and the SLT boresight is 120°, and the included angle between the plane of optical table and the SLT boresight is 37.76°. According to the installation configuration, the dihedral angle between the DM and the installation plane of SLT is 30°. Finally, the SLT can realize the imaging and monitoring of the laser. The power supply provides the SLT, the micro-motion table, and the laser sources with energy. The driver device is used to control the motion of the micro-motion table. The detailed information of the devices in the ground DSAP verification platform is listed in Table II.

Based on these devices, the ground DSAP verification platform is constructed, with which we can conduct the accuracy and effectiveness validation experiments.

B. Experiment Design

According to (10), the accuracy of the camera misalignment matrix $\boldsymbol{R}_{\text{cam},0}^{\text{cam},t}$ depends on the measurement accuracy of the original laser transformation matrix $\boldsymbol{T}_{\text{cam},0}^{\text{st}}$ and the received vector of laser source i in the SLT coordinate system at time t $\boldsymbol{w}_{i,t}^{k}$. $\boldsymbol{T}_{\text{cam},0}^{\text{st}}$ is calculated in the geometric calibration and is regarded as the constant zero point of monitoring for the next camera misalignment monitoring. Therefore, the error of $\boldsymbol{T}_{\text{cam},0}^{\text{st}}$ is the systematic deviation for the $\boldsymbol{R}_{\text{cam},0}^{\text{cam},t}$ monitoring. $\boldsymbol{w}_{i,t}^{k}$ is monitored and calculated in real time by (3). Thus, the error of $\boldsymbol{w}_{i,t}^{k}$ is the random error for the $\boldsymbol{R}_{\text{cam},0}^{\text{cam},t}$ monitoring.

With the ground DSAP verification platform, we capture two sets of image data, and each set contains 800 images. The first set is used as the calibration group for calculating $\boldsymbol{T}_{\text{cam},0}^{\text{st}}$ in the phase of geometric calibration. Another set is regarded as the monitoring group for updating $\boldsymbol{R}_{\text{cam},0}^{\text{cam},t}$ in real time. Furthermore, the assumed prerequisite of the experiment is that the structure of the platform is stable in a short time, which demonstrates that the real values of $\boldsymbol{T}_{\text{cam},0}^{\text{st}}$ and $\boldsymbol{R}_{\text{cam},0}^{\text{cam},t}$ are constant during the experiment. Therefore, the standard deviations (SDs) of the rotation angles decoupled from $\boldsymbol{T}_{\text{cam},0}^{\text{st}}$ and $\boldsymbol{R}_{\text{cam},0}^{\text{cam},t}$ are used for assessing the accuracy of the proposed method.

The difficulty in validating the effectiveness of the proposed method is to obtain the reference camera MA. The real thermal environment will bring the complex thermal deformation of the DSAP, of which the monitoring results are hard to be confirmed. According to (10), the translation of the camera focal plane can be equivalent to the camera misalignment angle, based on which effectiveness validation is possible. As for the telescope with 2000mm focal length, the micro-motion table with 100μm maximum travel can simulate an MA of approximately 10.3″.

To assess the effectiveness of the proposed method, the ground DSAP verification platform is set to continuous monitoring mode. Then, the micro-motion table is controlled to move in a certain step size and pattern. Based on the motion feedback value from the micro-motion table, the reference MA can be calculated by (10). Furthermore, the measurement value of the MA can be obtained by the proposed method. The difference between the reference MA and the measurement

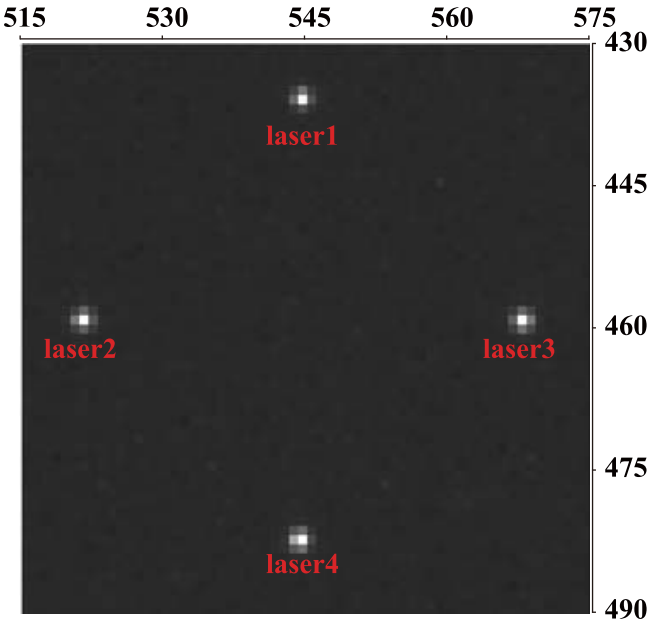

Fig. 7. Image region of the laser points in SLT image frame. The top and left tick marks indicate the pixel coordinates of the image region.

value can be used for assessing the effectiveness of the proposed method.

V. Results and Discussion

A. Laser Point Extraction Accuracy

The extraction of the laser point in SLT image frame is the foundation of the proposed method, and the extraction accuracy directly determines the accuracy of the camera misalignment model based on the "star–laser" joint detection. Therefore, the assessment of the extraction accuracy must be discussed.

The two sets of image data in the accuracy validation experiment are used for assessing the extraction accuracy. The assumed prerequisite of the extraction accuracy assessment is that the structure of the platform is stable during the experiment, which indicates that the extraction results of the laser points are constant in theory. The SDs of the coordinates of the four laser points are used for assessing the extraction accuracy.

Fig. 7 shows the image of the laser points in SLT. The imaging profiles of four laser points are similar to those of the stars. Most of the energy of the laser is concentrated within 5×5 pixels in the SLT detector. Therefore, the coordinates of the laser points are extracted by the center-of-gravity (CG) method, a typical and fast centroiding method [25].

After the extraction by the CG method, the coordinates of the laser points in SLT image frames are about (544.822, 435.751), (520.724, 459.788), (569.035, 459.876), and (544.579, 483.940). The SDs of the extracted coordinates from 800 images are listed in Table III and are about from 0.045 ps (3σ) to 0.060 ps (3σ). The extraction accuracy of the laser points is more excellent than that of the stars in the traditional star tracker, which is about 0.15–0.3 ps (3σ) in the real night sky observation. The reason for the higher accuracy of the laser extraction is thought to be that the optical path of the laser is more stable and is far from the interference of the external environment. Furthermore, the imaging position of the stars in star tracker is moving all the time, as shown in Fig. 1(c). The S-curve error and the blur caused by motion have a great influence on star extraction [26]. Thus, the profiles of the laser are more ideal, and the extraction accuracy is higher.

TABLE III
Extraction Accuracy of the Laser Points

Group ID	No. of laser	SDs of X position (pixels, 3σ)	SDs of X position (pixels, 3σ)
First Group	1	0.057	0.052
	2	0.051	0.050
	3	0.051	0.051
	4	0.045	0.052
Second Group	1	0.056	0.052
	2	0.046	0.049
	3	0.051	0.050
	4	0.045	0.048

B. Results of the Accuracy Validation Experiment

According to (7), the monitoring errors of the camera misalignment matrix contain the error of $\boldsymbol{T}^{\mathrm{st}}_{\mathrm{cam},0}$ and the error of $\boldsymbol{w}^{k}_{i,t}$. The former is the systematic deviation and the latter is the random error for the calculation of $\boldsymbol{R}^{\mathrm{cam},t}_{\mathrm{cam},0}$. Therefore, the errors of $\boldsymbol{T}^{\mathrm{st}}_{\mathrm{cam},0}$ and $\boldsymbol{R}^{\mathrm{cam},t}_{\mathrm{cam},0}$ are analyzed by the accuracy validation experiment.

The first group of 800 images is used for calculating and assessing the accuracy of $\boldsymbol{T}^{\mathrm{st}}_{\mathrm{cam},0}$. The emitted vectors of laser sources in the camera coordinate system $\boldsymbol{v}_{i,\mathrm{cam}}$ are obtained based on (2). The received vector of laser sources in the SLT coordinate system during the calibration phase $\boldsymbol{w}^{k}_{i,0}$ is obtained based on (3). Then, $\boldsymbol{T}^{\mathrm{st}}_{\mathrm{cam},0}$ is calculated. The value of $\boldsymbol{T}^{\mathrm{st}}_{\mathrm{cam},0}$ should be a constant value during the experiment (about 3 min). Hence, the average value of the calculated $\boldsymbol{T}^{\mathrm{st}}_{\mathrm{cam},0}$ from 800 images is regarded as the reference constant matrix. The errors of $\boldsymbol{T}^{\mathrm{st}}_{\mathrm{cam},0}$ can be obtained by multiplying the calculated $\boldsymbol{T}^{\mathrm{st}}_{\mathrm{cam},0}$ by the transposition of reference matrix. Then, the errors of $\boldsymbol{T}^{\mathrm{st}}_{\mathrm{cam},0}$ are shown in Fig. 8. It is worth noting that we only consider the accuracy of the errors in the X-/Y-directions because the errors of $\boldsymbol{T}^{\mathrm{st}}_{\mathrm{cam},0}$ in the Z-direction bring little impact on the imagery positioning and can be ignored.

The result shows that the calculation accuracy of $\boldsymbol{T}^{\mathrm{st}}_{\mathrm{cam},0}$ with single frame is about $1.16''$ (3σ) and $1.14''$ (3σ) in the X- and Y-directions, respectively. According to (6), the calculation of $\boldsymbol{T}^{\mathrm{st}}_{\mathrm{cam},0}$ is the same as the attitude determination of the star tracker. The attitude determination of the star tracker has been explained in [27] and is formulated as follows:

$$E_{X/Y} = \frac{\delta_{Y/X}}{\sqrt{N_{\mathrm{star}}}}\theta_{\mathrm{pixel}} \tag{11}$$

where $E_{X/Y}$ denotes the accuracy of the attitude matrix in the X- or Y-direction, $\delta_{X/Y}$ is the average centroiding accuracy

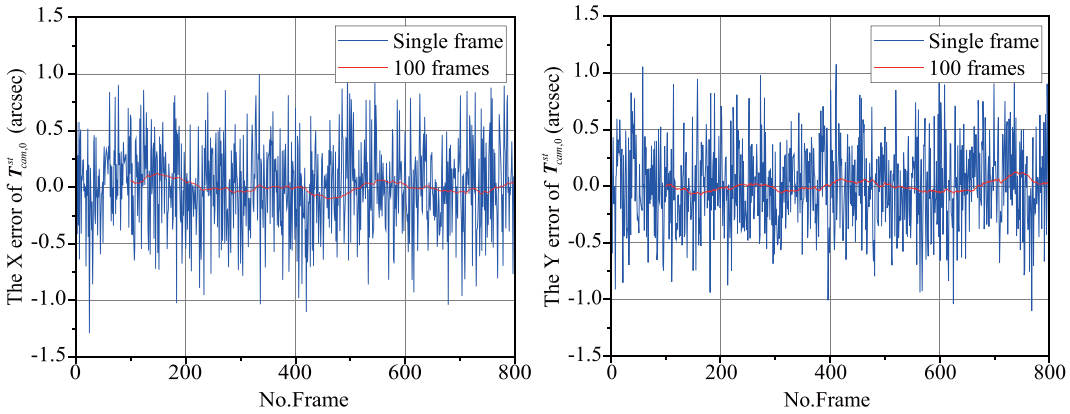

Fig. 8. Accuracy assessment of $\boldsymbol{T}^{\mathrm{st}}_{\mathrm{cam},0}$ in the X-direction (left) and Y-direction (right). The blue line denotes the calculated MA of $\boldsymbol{T}^{\mathrm{st}}_{\mathrm{cam},0}$ with single frame. The red line denotes the smoothed MA of $\boldsymbol{T}^{\mathrm{st}}_{\mathrm{cam},0}$ with 100 frames.

TABLE IV
ACCURACY OF THE MATRIX WITH DIFFERENT FRAMES

Frame	The accuracy of the $T^{st}_{cam,0}$		The accuracy of the $R^{cam,t}_{cam,0}$	
	X direction (arcsec, 3σ)	Y direction (arcsec, 3σ)	X direction (arcsec, 3σ)	Y direction (arcsec, 3σ)
1	1.16	1.14	1.14	1.15
4	0.59	0.59	0.58	0.56
16	0.33	0.31	0.30	0.27
25	0.26	0.25	0.24	0.20
49	0.21	0.18	0.20	0.15
100	0.14	0.13	0.15	0.11

of imaging points, N_{star} is the number of imaging points, and θ_{pixel} is the angular resolution.

Equation (11) can also explain the accuracy of $\boldsymbol{T}^{\mathrm{st}}_{\mathrm{cam},0}$. The average centroiding accuracy of the laser points is about 0.051 ps (3σ). The angular resolution of the SLT is about $44.6''$ and the number of the detected laser points is 4. The estimation accuracy by (11) is nearly consistent with the measurement accuracy.

Considering that $\boldsymbol{T}^{\mathrm{st}}_{\mathrm{cam},0}$ is stable during the experiment, we can use the laser points from continuous image sequence for the calculation, which can increase the number of the detected laser points and improve the accuracy according to (11). Actually, the calculation with the continuous image sequence is the operation of smooth filtering for suppressing the influence of the centroiding error of the laser points. In the method, the number of images is set to 100 (about 22s). Then, the errors of $\boldsymbol{T}^{\mathrm{st}}_{\mathrm{cam},0}$ are about within $\pm 0.14''$ in both X- and Y-directions, which is also nearly consistent with (11). In order to prove the correctness of (11), the accuracy of $\boldsymbol{T}^{\mathrm{st}}_{\mathrm{cam},0}$ and the number of images are listed in Table IV.

The second group of 800 images is used to monitor and validate the accuracy of the camera misalignment $\boldsymbol{R}^{\mathrm{cam},t}_{\mathrm{cam},0}$. $\boldsymbol{T}^{\mathrm{st}}_{\mathrm{cam},0}$ is obtained by the first group. The received vector of laser sources in the SLT coordinate system during the monitoring phase at time t $\boldsymbol{w}^k_{i,t}$ is obtained by the coordinates of the laser points in the 800 images of the second group. The camera misalignment matrix $\boldsymbol{R}^{\mathrm{cam},t}_{\mathrm{cam},0}$ can be calculated by (7). Then, the MA can be obtained and is shown in Fig. 9. The result shows that the monitoring accuracy of $\boldsymbol{R}^{\mathrm{cam},t}_{\mathrm{cam},0}$ with single frame is about $1.14''$ (3σ) and $1.15''$ (3σ) in the X- and Y-directions, respectively. The accuracy of $\boldsymbol{R}^{\mathrm{cam},t}_{\mathrm{cam},0}$ is similar to that of $\boldsymbol{T}^{\mathrm{st}}_{\mathrm{cam},0}$ and follows the relationship formulated by (11). Because of the difference of the camera alignment matrix between the first group and the second group, the MAs are not near zeros. Then, the errors of $\boldsymbol{R}^{\mathrm{cam},t}_{\mathrm{cam},0}$ with 100 images are also about within $\pm 0.15''$ in both X- and Y-directions. The monitoring accuracy of the misalignment matrix $\boldsymbol{R}^{\mathrm{cam},t}_{\mathrm{cam},0}$ and the number of images are also listed in Table IV.

C. Results of the Effectiveness Validation Experiment

The accuracy of the proposed method is analyzed by the above accuracy validation experiment. However, it is hard to prove the effectiveness of the proposed method, which should be estimated by the difference between the reference MA and the measured MA. According to (10), the motion value of the camera focal plane can simulate the camera misalignment. Hence, we utilize the micro-motion table for precisely controlling the motion of the camera focal plane. The motion value can be obtained by the control software of the micro-motion table, based on which the reference MA is calculated. Then, the monitoring MA is obtained by the proposed method. Thus, the difference between the reference value and the monitoring value can be used for evaluating the effectiveness of the proposed method.

As for the experiment, the position of the micro-motion table is set to 10μm at first. Meanwhile, the ground DSAP verification platform is set to the monitoring status. Then, the micro-motion table is controlled to move from 10 to 90μm with a step of 20μm in the X- and Y-directions at the same time, as shown in Fig. 10(a). The micro-motion table can provide the position value of each motion state. At least 400 images (about 90s) are captured during each motion state. The images of the first motion state are used to calculate $\boldsymbol{T}^{\mathrm{st}}_{\mathrm{cam},0}$ as the zero point of MA monitoring. Then, the images of other motion states are used for monitoring MA by the proposed method. The reference results of MA can be calculated based on (10). To validate the effectiveness of the proposed method,

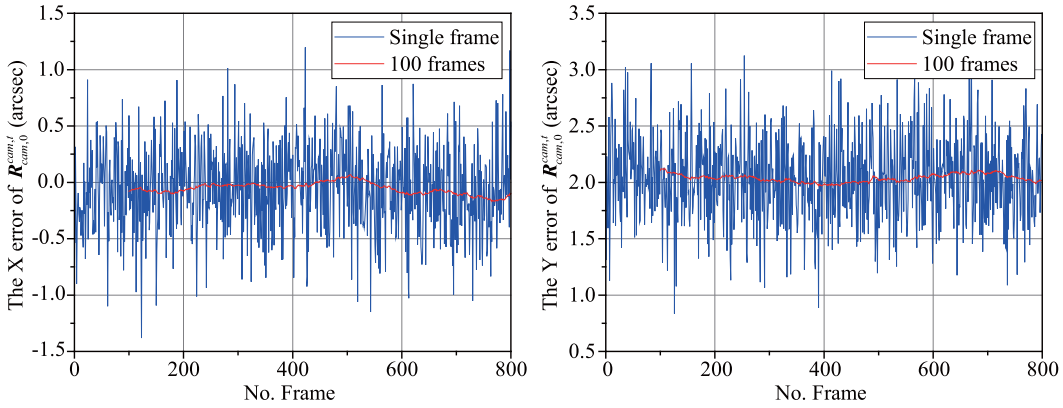

Fig. 9. Accuracy assessment of $\boldsymbol{R}_{\text{cam},0}^{\text{cam},t}$ in the X-direction (left) and Y-direction (right). The blue line denotes the calculated MA of $\boldsymbol{R}_{\text{cam},0}^{\text{cam},t}$ with single frame. The red line denotes the smoothed MA of $\boldsymbol{R}_{\text{cam},0}^{\text{cam},t}$ with 100 frames.

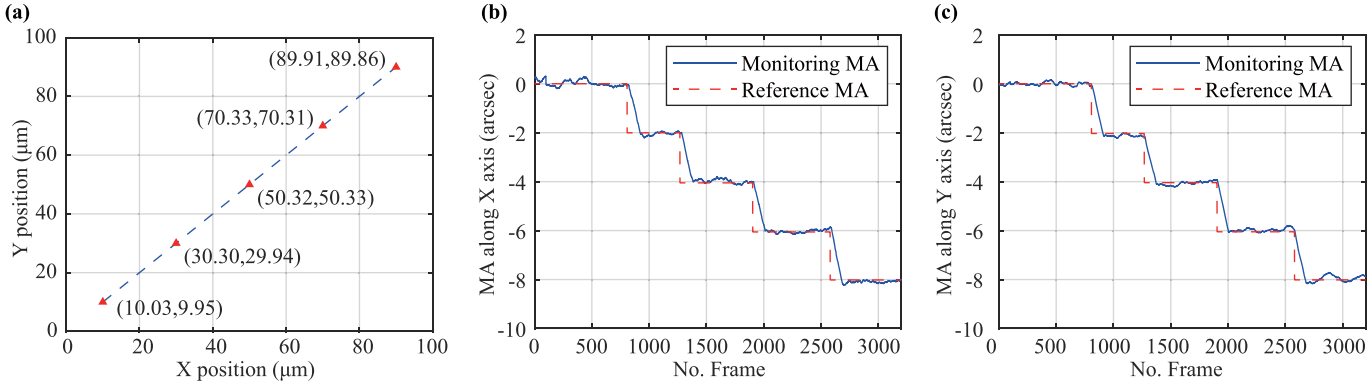

Fig. 10. (a) Motion pattern of the micro-motion table. The red triangle markers denote the five motion states of the micro-motion table, and the position values are obtained from the micro-motion table. (b) Monitoring results of MA when the micro-motion table moves in the X-direction. The blue line indicates the monitoring MA, and the red dashed line denotes the reference MA calculated by the motion values from the micro-motion table. (c) Monitoring results of MA when the micro-motion table moves in the Y-direction.

TABLE V
REFERENCE AND MONITORING RESULTS OF MA

State	Micro-motion table moves in X direction					Micro-motion table moves in Y direction				
	Position (μm)	**Motion value (μm)**	**Reference MA along Y-axis (arcsec)**	**Monitoring MA along Y-axis (arcsec)**	**Difference (arcsec)**	**Position (μm)**	**Motion value (μm)**	**Reference MA along X-axis (arcsec)**	**Monitoring MA along X-axis (arcsec)**	**Difference (arcsec)**
1	10.03	0	-	-	-	9.95	0	-	-	-
2	30.30	20.27	-2.006	-2.046	**-0.040**	29.94	19.99	-2.034	-2.125	**-0.091**
3	50.32	40.29	-4.051	-3.978	**0.073**	50.33	40.38	-4.042	-4.070	**-0.028**
4	70.33	60.30	-6.056	-6.032	**0.024**	70.31	60.66	-6.050	-5.972	**0.078**
5	89.91	79.88	-8.017	-8.089	**-0.072**	89.86	79.91	-8.014	-7.955	**0.059**

the average value of the measured MA during each motion state is compared with the reference value.

The real-time monitoring results of MA along the X- and Y-axes are shown in Fig. 10(b) and (c), respectively. The monitoring results of MA show good agreement with the change of the reference MA. The micro-motion table changes the position in a very short time. Hence, the reference MA undergoes a sudden change with the motion of micro-motion table. The monitoring MA is obtained by fusing the data of 100 consecutive images. Therefore, the monitoring MA cannot keep up with the sudden change of the reference MA at once. Actually, the misalignment change of camera on orbit is a slowly varying process. Compared with the change time of camera misalignment, the time of capturing 100 consecutive images is very short. To further describe the experiment, the detailed results are listed in Table V. The motion value can be obtained by subtracting the position value of the first motion state from that of the current motion state. The reference MA can be obtained by (10), and the motion direction of the micro-motion table is orthogonal to the rotation direction of the camera misalignment. The monitoring MA is the average value of the measured MA during each motion state.

As shown in Table V, the differences between reference MA and monitoring MA are within $\pm 0.1''$. It demonstrates that the method can effectively and accurately monitor the camera misalignment, which is the low-frequency error component in the attitude determination of camera. By monitoring and compensating for the camera misalignment, the attitude determination accuracy of camera can be improved. Then, the high-accuracy geometric positioning will also be guaranteed.

D. Analysis of the Optimal Design for Angular Resolution

As shown in (11), when the number of the laser spot remains unchanged, the monitoring accuracy of camera misalignment is related to the angular resolution of the SLT and the centroiding accuracy. To ensure the optimal effect of our work, we analyzed the ideal optimal design for the angular resolution of the SLT in our experiment platform. In our experiment platform, the number of the laser spot is 4 and the energy of laser spot is mainly within 5×5 pixels, as shown in Fig. 7. Therefore, the physical radius of laser spot is set to 7.5μm (about 0.58 ps@13μm), and we keep the laser spot radius unchanged in the analysis. According to the previous studies [26], under the condition that the imaging spot radius in the detector remains constant, the angular resolution and centroiding accuracy interact with each other. Therefore, the comprehensive impact of centroiding accuracy and the angular resolution should be analyzed.

Then, we conduct a numerical simulation experiment to explain the relationship between the angular resolution and the centroiding accuracy. In the numerical simulation, the centroiding method is the CG method. The parameters of the Gaussian function of the laser spot are set to close to those measured in our experiment. It is worth noting that the laser position is not stationary. We assume that the positions of laser spot are evenly distributed within one pixel (from -6.5 to 6.5μm). The distribution range of the laser spot is subdivided into 50 phases. The Gaussian functions of laser spot with 50 phases are integrated to simulate the ideal light signal. Then, the Poisson noise is added according to the noise model introduced in EMVA 1288 Standard [28] and Zhan et al. [26]. The parameters of the noise are also close to those measured in our experiment.

The angular resolution of pixel is set from $10''$ to $80''$. Under the conditions of each angular resolution, the 50 phases of laser spot are all considered. For each phase, the centroiding results of laser spot are obtained through 500 Monte Carlo simulations. Then, we can obtain the relationship between the angular resolution and the centroiding accuracy of CG method, and the relationship between the angular resolution and the monitoring accuracy calculated by (11), which are shown in Fig. 11.

As shown in Fig. 11(a), the improvement of angular resolution may cause the degradation of centroiding accuracy. Under the conditions of numerical simulation, when the angular resolution is $43''$ (the Gaussian radius of laser spot is about 0.6 ps), the centroiding accuracy is best and can achieve 0.016 ps (1σ). As shown in Fig. 11(b), the improvement of angular resolution can upgrade the monitoring accuracy of camera misalignment. However, when the angular resolution is less than $40''$, the upgradation of accuracy is not significant. Therefore, the results demonstrate that the design for the angular resolution in the SLT of our experiment platform is close to optimal.

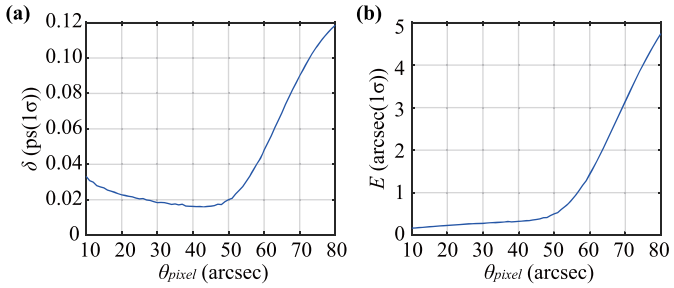

Fig. 11. (a) Relationship between the angular resolutiom θ_{pixel} and the centroiding accuracy δ. (b) Relationship between the angular resolution θ_{pixel} and the monitoring accuracy of camera misalignment E calculated by (11).

VI. Conclusion

In this article, we build an active fiducial optical path between camera and SLT to couple the imagery positioning with the attitude determination. Then, the attitude determination and imagery positioning model based on "star–laser" joint detection is established for monitoring and correcting the time-variant camera misalignment, which is the main obstacle for actualizing the high-accuracy imagery positioning. Ground experimental results show that the proposed method can accurately and effectively monitor the misalignment and provide the possibility of maintaining high-accuracy camera inertial attitude in real time. At present, the main limitation of this work is that the effectiveness of the proposed method has not been revalidated through the on-orbit star images. The next step of this research is to conduct the on-orbit experiment to validate the performance of the proposed method in monitoring the camera misalignment in real time and realizing imagery positioning with high accuracy. Therefore, the data transmission serial port and the sufficient downlink bandwidth of the star images have been set in the SVGF-1 satellite to ensure the implementation of the on-orbit validation experiment.

Acknowledgment

The authors declare that they have no known competing financial interests or personal relationships that could appear to influence the work reported in this article.

References

[1] A. H. Pickens et al., "Mapping and sampling to characterize global inland water dynamics from 1999 to 2018 with full Landsat time-series," *Remote Sens. Environ.*, vol. 243, Jun. 2020, Art. no. 111792, doi: 10.1016/j.rse.2020.111792.

[2] J. J. Dalcanton, "18 years of science with the Hubble space telescope," *Nature*, vol. 457, no. 7225, pp. 41–50, Jan. 2009, doi: 10.1038/nature07621.

[3] J. Li, F. Xing, D. Chu, and Z. Liu, "High-accuracy self-calibration for smart, optical orbiting payloads integrated with attitude and position determination," *Sensors*, vol. 16, no. 8, p. 1176, Jul. 2016, doi: 10.3390/s16081176.

[4] T. Wang et al., "Geometric accuracy validation for ZY-3 satellite imagery," *IEEE Geosci. Remote Sens. Lett.*, vol. 11, no. 6, pp. 1168–1171, Jun. 2014, doi: 10.1109/lgrs.2013.2288918.

[5] B. Yang, M. Wang, W. Xu, D. Li, J. Gong, and Y. Pi, "Large-scale block adjustment without use of ground control points based on the compensation of geometric calibration for ZY-3 images," *ISPRS J. Photogramm. Remote Sens.*, vol. 134, pp. 1–14, Dec. 2017, doi: 10.1016/j.isprsjprs.2017.10.013.

[6] M. Wang, Y. Cheng, X. Chang, S. Jin, and Y. Zhu, "On-orbit geometric calibration and geometric quality assessment for the high-resolution geostationary optical satellite GaoFen4," *ISPRS J. Photogramm. Remote Sens.*, vol. 125, pp. 63–77, Mar. 2017, doi: 10.1016/j.isprsjprs.2017.01.004.

[7] Y. Wang, M. Wang, Y. Zhu, and X. Long, "Low frequency error analysis and calibration for multiple star sensors system of GaoFen7 satellite," *Geo-Spatial Inf. Sci.*, pp. 1–13, Sep. 2022, doi: 10.1080/10095020.2022.2100284.

[8] *The Datasheet of High-Accuracy Star Sensor Production*. [Online]. Available: http://www.ty-space.com/en/

[9] R. Gachet, "SPOT5 in-flight commissioning: Inner orientation of HRG and HRS instruments," in *Proc. 20th ISPRS Congr., Commun.*, Istanbul, Turkey, vol. 35, 2004, pp. 1–5.

[10] D. Greslou, F. de Lussy, J. M. Delvit, C. Dechoz, and V. Amberg, "Pleiades-HR innovative techniques for geometric image quality commissioning," *Int. Arch. Photogramm., Remote Sens. Spatial Inf. Sci.*, vols. 39, pp. 543–547, Jul. 2012.

[11] A. Bouillon, E. Breton, F. De Lussy, and R. Gachet, "SPOT5 HRG and HRS first in-flight geometric quality results," *Proc. SPIE*, vol. 4881, pp. 212–223, Apr. 2003.

[12] G. Dial, H. Bowen, F. Gerlach, J. Grodecki, and R. Oleszczuk, "IKONOS satellite, imagery, and products," *Remote Sens. Environ.*, vol. 88, nos. 1–2, pp. 23–36, Nov. 2003, doi: 10.1016/j.rse.2003.08.014.

[13] J. Grodecki and G. Dial, "IKONOS geometric accuracy validation," *Int. Arch. Photogram. Remote Sens. Spatial Inf. Sci.*, vol. 34, no. 1, pp. 50–55, 2002.

[14] Y. Zhang, M. Zheng, J. Xiong, Y. Lu, and X. Xiong, "On-orbit geometric calibration of ZY-3 three-line array imagery with multistrip data sets," *IEEE Trans. Geosci. Remote Sens.*, vol. 52, no. 1, pp. 224–234, Jan. 2014, doi: 10.1109/tgrs.2013.2237781.

[15] X. Chen, F. Xing, Z. You, X. Zhong, and K. Qi, "On-orbit high-accuracy geometric calibration for remote sensing camera based on star sources observation," *IEEE Trans. Geosci. Remote Sens.*, vol. 60, 2022, Art. no. 5608211, doi: 10.1109/tgrs.2021.3100841.

[16] J. Takaku and T. Tadono, "PRISM on-orbit geometric calibration and DSM performance," *IEEE Trans. Geosci. Remote Sens.*, vol. 47, no. 12, pp. 4060–4073, Dec. 2009, doi: 10.1109/tgrs.2009.2021649.

[17] X. Li, L. Yang, X. Su, Z. Hu, and F. Chen, "A correction method for thermal deformation positioning error of geostationary optical payloads," *IEEE Trans. Geosci. Remote Sens.*, vol. 57, no. 10, pp. 7986–7994, Oct. 2019, doi: 10.1109/tgrs.2019.2917716.

[18] J. Wang, R. Wang, X. Hu, and Z. Su, "The on-orbit calibration of geometric parameters of the Tian–Hui 1 (TH-1) satellite," *ISPRS J. Photogramm. Remote Sens.*, vol. 124, pp. 144–151, Feb. 2017, doi: 10.1016/j.isprsjprs.2017.01.003.

[19] J. Wang and R. Wang, "EFP multi-functional bundle adjustment of mapping Satellite-1 without ground control points," *J. Remote Sens.*, vol. 16, no. 1, pp. 112–115, 2012.

[20] J. Li, R. Wang, L. Zhu, and H. Huang, "In-flight geometric calibration for mapping Satellite-1 surveying and mapping camera," *J. Remote Sens.*, vol. 16, no. 1, pp. 35–39, 2012.

[21] S. Bae et al., "Performance of ICESat-2 precision pointing determination," *Earth Space Sci.*, vol. 8, no. 4, Apr. 2021, Art. no. e2020EA001478, doi: 10.1029/2020ea001478.

[22] J. M. Sirota et al., "The transmitter pointing determination in the geoscience laser altimeter system," *Geophys. Res. Lett.*, vol. 32, no. 22, pp. 1–4, Nov. 2005, Art. no. L22S11, doi: 10.1029/2005gl024005.

[23] M. D. Shuster, "The quest for better attitudes," *J. Astron. Sci.*, vol. 54, nos. 3–4, pp. 657–683, Dec. 2006, doi: 10.1007/BF03256511.

[24] M. D. Shuster and S. D. Oh, "Three-axis attitude determination from vector observations," *J. Guid. Control*, vol. 4, no. 1, pp. 70–77, Jan. 1981, doi: 10.2514/3.19717.

[25] R. C. Stone, "A comparison of digital centering algorithms," *Astronomical J.*, vol. 97, no. 4, pp. 1227–1237, Apr. 1989, doi: 10.1086/115066.

[26] H. Zhan et al., "Analyzing the effect of the intra-pixel position of small PSFs for optimizing the PL of optical subpixel localization," *Engineering*, Apr. 2023, doi: 10.1016/j.eng.2023.03.009.

[27] C. C. Liebe, "Accuracy performance of star trackers—A tutorial," *IEEE Trans. Aerosp. Electron. Syst.*, vol. 38, no. 2, pp. 587–599, Apr. 2002.

[28] *Standard for Characterization of Image Sensors and Cameras Release 3.1*, Standard EMVA 1288, 2016.

Xuedi Chen (Graduate Student Member, IEEE) was born in 1997. He received the B.S. degree in measurement and control technology and instrument from the School of Precision Instrument and Opto-Electronics Engineering, Tianjin University, Tianjin, China, in 2018. He is currently pursuing the Ph.D. degree with the Department of Precision Instrument, Tsinghua University, Beijing, China.

He majors in geometry processing of spaceborne optical imagery.

Haiyang Zhan was born in 1996. He received the B.S. degree in automation from the Beijing Institute of Technology, Beijing, China, in 2017. He is currently pursuing the Ph.D. degree with the Department of Precision Instrument, Tsinghua University, Beijing.

His research focuses on high-precision optical measurement.

Shaoyan Fan was born in 1996. He received the B.S. degree in mechanical engineering and automation from the Dalian University of Technology, Dalian, China, in 2018. He is currently pursuing the Ph.D. degree with the Department of Precision Instrument, Tsinghua University, Beijing, China.

His research focuses on high-accuracy determination and control of attitude.

Qilong Rao received the B.S. degree from the Nanjing University of Aeronautics and Astronautics, Nanjing, China, in 2005, and the M.S. degree in electronic and communication engineering from Shanghai Jiaotong University, Shanghai, China, in 2012.

After graduation, he devoted himself to the overall design of optical remote sensing satellites. In 2015, he obtained the title of senior engineer.

Zhenqiang Hong received the B.S. degree from Beihang University, Beijing, China, in 2012, and the M.S. degree in aeronautical and astronautical science and technology from the Shanghai Academy of Spaceflight Technology, Shanghai, China, in 2015. He is currently pursuing the Ph.D. degree with the College of Aerospace Engineering, Nanjing University of Aeronautics and Astronautics, Nanjing, China.

His research focuses on the overall design of optical remote sensing satellites.

Zheng You received the B.S., M.S., and Ph.D. degrees from the Huazhong University of Science and Technology, Wuhan, China, in 1985, 1987, and 1990, respectively.

After graduation, he joined the Faculty of the Department of Precision Instruments and Mechanology, Tsinghua University, Beijing, China, as an Assistant Professor. He became an Associate Professor in 1992 and a Full Professor in 1994. In 2015, he was the Vice President of Tsinghua University. In 2022, he became the President of the Huazhong University of Science and Technology. He has published more than 300 articles and 32 research reports. He holds 12 Chinese invention patents. His main research interests include micro–nano technology and micro–nano satellite technology.

Dr. You was awarded the specially appointed Professor for Chang Jiang Scholar from the Ministry of Education in 2001 and the Academician by the Chinese Academy of Engineering in 2013.

Fei Xing received the B.S. degree in mechanical engineering from Tongji University, Shanghai, China, in 2002, and the Ph.D. degree from Tsinghua University, Beijing, China, in 2006.

After graduation, he joined the Faculty of the Department of Precision Instruments and Mechanology, Tsinghua University, as an Assistant Researcher. He became an Associate Professor in 2011 and a Full Professor in 2021. He has published more than 70 articles. His main research interests include micro-miniature high-precision attitude measurement sensor technology.

Dr. Xing was awarded the specially appointed Professor for Chang Jiang Scholar from the Ministry of Education in 2020 and the Xplorer Prize from the Tencent Foundation in 2021.

Chunyu Liu received the B.S. degree from Jilin University, Changchun, China, in 2005, and the Ph.D. degree from the Changchun Institute of Optics, Fine Mechanics and Physics, Chinese Academy of Sciences, Changchun, in 2011.

She is currently a Ph.D. Supervisor and a Researcher with the Changchun Institute of Optics, Fine Mechanics and Physics, Chinese Academy of Sciences. She mainly engages in the research of optical system design and overall design of optic-electronic systems.